# DBD Plasma-Based Stall Control on a General Aviation Scale Model

**Preprint** · February 2025

DOI: 10.13140/RG.2.2.28663.94882



David Greenblatt
Technion – Israel Institute of Technology

# DBD Plasma-Based Stall Control on a General Aviation Scale Model


Mordechai Garcia,*

*Technion – Israel Institute of Technology, Technion City, Haifa 3200003, Israel*

Michael Mongin†

*U.S. Air Force Research Laboratory, Wright-Patterson Air Force Base, OH 45433, USA*

David Greenblatt‡

*Technion – Israel Institute of Technology, Technion City, Haifa 3200003, Israel*



Wind tunnel and flight experiments were performed on a general aviation 6.1:1 scale model, where pulse-modulated dielectric barrier discharge (DBD) plasma actuators were used to control wing stall. Plasma actuation on the unpowered model produced modest increases in maximum lift coefficient, while post-stall lift coefficients never dropped below the baseline (non-actuated) maximum. Flow visualization revealed that actuation fully attached the outboard flow while also preventing inboard leading-edge stall. Powered wind tunnel tests showed that the propeller wake promotes, or exacerbates, separation at post-stall angles of attack, but these effects are partially overcome by actuation, which delivers a 6% reduction in stall speed. Flight experiments, performed while gliding, showed that actuation dramatically reduces uncontrolled pitch, roll and yaw, and loss of altitude. By preventing massive separation, actuation facilitates safe and stable flight at angles of attack at, and greater than, the baseline static stall angle. The DBD plasma stall control system can easily be retrofitted to a full-scale general aviation aircraft, or integrated into the wing design.



* Graduate Student, Faculty of Mechanical Engineering.

† Aerospace Researcher, Aerospace Systems Directorate, AIAA Young Professional Member.

‡ Professor, Louis and Helen Rogow Chair in Aeronautical Engineering. Faculty of Mechanical Engineering, AIAA Associate Fellow, davidg@technion.ac.il (corresponding author).

## Nomenclature

$AR$ = aspect ratio, $b/\bar{c}$

$b$ = wing span (m)

$\bar{c}$ = average wing chord-length (m)

$C_D$ = drag coefficient, $F_D/qS$

$C_{D0}$ = zero-lift base-drag coefficient

$C_L$ = lift coefficient, $F_L/qS$

$C_\mu$ = plasma body force coefficient, $F'_B/qc$

$f_p$ = plasma pulse-modulation frequency (Hz)

$F^+$ = blade reduced frequency, $f_p\bar{c}/U$

$F'_B$ = plasma body force per unit span

$P$ = power supplied to the motor (W)

$P_{pl}$ = power supplied to the actuators (W)

$q$ = dynamic pressure, $\frac{1}{2}\rho U^2$ (Pa)

$Re$ = Reynolds number, $U\bar{c}/\nu$

$S$ = wing planform area ($m^2$)

$U$ = wind tunnel freestream and flight speed (m/s)

$V$ = voltage (V)

$V_{\mathrm{pp}}$ = peak-to-peak voltage (kV)

$\alpha$ = angle-of-attack (°)

$\alpha_s$ = stall angle-of-attack (°)

$\delta$ = inboard-flap deflection angle (°)

# I. Introduction

Stall on fixed-wing aircraft occurs when the angle-of-attack exceeds a critical value, denoted by the stall angle $\alpha_s$, and is characterized by a loss of lift and, in many cases, control. On conventional subcritical unswept wings, stall is initiated by boundary layer separation from the surface that results from a pressure rise along the chord. Conventional flight is generally restricted to flight speeds that exceed the corresponding stall speed—for example, during takeoff, landing and loiter, typical safety regulations demand a minimum flight speed that is 20% higher than the stall speed [1]. The safety margin allows pilots or automatic flight controllers to avoid stall and maintain control, but stall-related accidents have not been eliminated. Two recent surveys found that wing stall still accounts for approximately 12% of general aviation (GA) accidents, and that fatalities resulting from stall-induced accidents during the last six decades have remained consistently high, at approximately 40% [2-4].

Apart from improvements in flight training, designers attempt to design wings that have greater resistance to stall. This is usually done via design of the profile or planform [5] or by some sort of flow separation control device. The most common and widely used stall control device is the vortex generator (VG) [6,7]. VGs are small vanes that are attached to the wing in an oblique manner, often in symmetric pairs, and produce streamwise vortices that transport high-momentum flow towards the surface, rendering the flow less prone to separation. They can be, and often are, retrofit to aircraft wings and flaps, but they only operate in a narrow band of flight conditions which limits control authority, and they add drag at cruise conditions [6,7]. The latter can be offset by developing “on demand” VGs, for example, deployable VGs using Shape Memory Alloys (SMAs) [8,9] or rotatable VGs using servo motors [10]. However, this does not solve the problem of control authority, and for this we must turn to active flow control (AFC) methods.

Many AFC techniques, such as slot blowing [11], synthetic jets [12], or fluidic vortex generators [13] are known to be effective for stall control. However, they require major wing design modifications, the addition of electro-mechanical systems, or internal plumbing. A relatively simple and well-known stall-control device is the dielectric barrier discharge (DBD) plasma actuator [14,15]. It consists of a dielectric material and two electrodes—one encapsulated and one exposed—arranged asymmetrically. DBD actuators can be integrated into the profile geometry [16] or attached to the surface using an adhesive [17]. An Alternating Current (AC) waveform, from a few kilovolts to tens of kilovolts peak-to-peak $(V_{\mathrm{pp}})$, is typically applied to the electrodes in the ionization frequency range $f_{\mathrm{ion}} = \mathcal{O}(10^3)$ to $\mathcal{O}(10^4)$ Hz, between the electrodes. Pulse-modulation of the ionization frequency at a lower frequency $f_p$ achieves two objectives. First, it is selected to correspond to a known flow instability that is receptive to active perturbations; and second, it can be operated at a very low duty cycle (d.c.), even a few percent, which results in a proportional power saving [18]. When attached to the leading-edge of an airfoil or wing, actuation can either delay flow separation to higher angles-of-attack or attach an otherwise separated flow. Actuation usually produces a modest increase in $C_{L,\max}$ and a significant increase in post-stall $C_L$ (see references in [17]), essentially preventing leading-edge stall up to large post-stall angles of attack. Excitation of the airfoil separation bubble or the freestream shear layer is commonly characterized by the reduced frequency:

$$F^{+} \equiv \frac{f_p c}{U_\infty} \tag{1}$$

It has been determined empirically that excitation is effective for lift enhancement over the range $0.3 \lesssim F^{+} \lesssim 5$ [12] and up to large post-stall angles of attack. Reduced frequencies up to $F^{+} = 50$ are also effective, but they have proportionally higher power consumption and a smaller effect on lift hysteresis at deep stall angles of attack [19].

In contrast to the relatively large number of wind tunnel experiments, very few flight experiments have been performed (see [20-24] in Table 1). The initial demonstration of plasma actuators on the leading-edge of a sailplane was performed by Sidorenko et al. [20], who observed changes to the boundary layer. Grundmann et al. [21] applied actuators to a model with a near-elliptic planform, and reported a reduction in stall speed. More recent flight experiments by Su et al. [23] and Sekimoto et al. [24] confirmed these findings; furthermore, it was shown that actuation can be differentially applied to achieve rolling moments greater than those achieved by 20° aileron deflections [23].

**Table 1. Summary of flight experiments with DBD plasma actuators employed for separation control.**

| ref. | platform | profile | $b$ (m) | Plasma | config. | dielectric, $t_d$ | nom. $F^+$ | $V_{pp}$ (kV) | main result |
|---|---|---|---|---|---|---|---|---|---|
| [20] | SZD-48 Jantar sailplane | NN-8 | 15 | AC-DBD | one wing inboard, upwind-facing at LE | polyvinyl chloride 240 µm | ~70 | 10 | effect on tufts at the trailing-edge |
| [21] | custom tractor, near-elliptical planform | Clark-Y | 1.8 | AC-DBD | both wings outboard, 450 mm | (not reported) | ~2.1 | 10.5 | reduction is stall speed |
| [22] | custom, two pusher props | HQ/W 2,5/15 | 2.38 | AC-DBD | upstream of separation ramps | Kapton tape 350 µm | 0.3 to 1.4 | ~14 | implementation of flight control system |
| [23] | amphibious aircraft | NACA 23018 and 4412 | 2.87 | pulsed DC | both wings, midspan and outboard, 1,000 mm | Kapton tape 200 µm | 1.0 | 10 | 10.4% maximum lift coefficient increase |
| [24] | Voltantex RC Ranger EX | Clark-Y | 1.98 | AC-DBD | both wings, outboard mounted, 400 mm | polyimide 180 µm | 6.7 | ~8 | observed stall delay |

Another aspect of stall control has not received attention is DBD plasma effectiveness in the wake of a propeller, i.e., over wings subjected to propwash. This is an important factor because many general aviation (GA) aircraft wings are designed with washout (e.g., downward blade twist from root to tip) or outboard sweep, that ensures stall inboard stall (near the root) so as to retain aileron effectiveness [5]. The result is that the wing stalls initially inboard in the wake of the propeller. Due to the multitude of tractor-type aircraft configurations, the aerodynamic interference between propellers and wings has been extensively studied, particularly under cruise conditions [25-29]. The combination of axial and swirling velocities significantly affects the local lift distribution, and hence the wings' aerodynamic performance. Propeller upwash over the inboard part of the wing counteracts well-known finite-wing downwash to increase the local angle-of-attack, increase the section lift and reduce conventional induced drag. Very little research appears to have been done at or beyond the static stall angle. One exception is [27], where the propeller pitch angle was maintained at 0°, while the wing angle-of-attack was varied. Close to the stall angle, the effects on induced drag were minimal and stall was promoted at low propeller advance ratios (high-power). It is most likely that increases in the local angle-of-attack due to upwash promoted separation. To the best knowledge of the authors, the efficacy of DBD plasma actuation for stall control within the propwash region has not been studied.

The global objective of this research is to develop an automated closed-loop DBD plasma stall control system, that can be retrofitted to GA aircraft. In this research, proof-of-concept experiments were performed using a battery-powered 6.1:1 scale GA model. The first objective was to evaluate the effect of open-loop DBD plasma actuation on the full model by means wind tunnel experiments, under unpowered and powered conditions. The second objective was to conduct unpowered flight experiments while recording flight data, in order to demonstrate the effectiveness stall control in flight. The third, and final, objective was to determine the system requirements for full-scale aircraft implementation and automatic control. The remainder of the paper is structured as follows: Section II describes the flight model and experimental configurations; section III discusses the unpowered and powered tunnel wind tunnel results; section IV describes the results of a typical flight experiment; section VI presents the requirements for full-scale aircraft implementation and automatic control; and VI summarizes the main conclusions.

## II. Experimental Configurations & Methods

### A. The Flight Model

The flight model selected for this study is a battery-powered FMS Ranger PNP radio controlled (RC) model, powered by a 3541-750Kv brushless motor and a 12×7.5 two-bladed propeller (see Fig. 1, left). It is based on a 6:1 Cessna 172 geometry, with a length of 1.32 m, a wingspan $b = 1.8$ m, an aspect ratio $AR = 7.1$, and Clark-Y wing-profiles with inboard flaps. The total unmodified weight with battery is $W_0 = 2.18$ kg. Unlike the full-scale aircraft that employs a modified NACA 2412 wing section, the model section is similar to a GOE 702 airfoil, whose thickness is scaled by a factor of 0.6702. Access hatches, for the plasma system hardware, were cut into the left side of the fuselage and the resulting frame was reinforced with carbon fiber strips (see Fig. 2).

Plasma actuators, constructed using 50 μm thick copper electrodes and a 0.4 mm thick silicone rubber dielectric, were mounted along the full extent of the wingspan (see Fig. 1, left). High-voltage signals were supplied by means of a commercially available Minipuls 0.1® (GBS Elektronik) generator with a 12-kV peak-to-peak capability in the frequency range 5 - 20 kHz (see Fig. 2). The assembly consists of a full bridge converter and a transformer cascade, with a total mass of 360 grams. Power is supplied by an 11.1-volt lithium-polymer battery, via a 30-volt step-up boost-converter. Burst frequency $f_p$, duty cycle (d.c.) and phase are preset by board-mounted trimpots. Radio controlled activation of the plasma signal is achieved by means of a microswitch that is activated by a small servo-mounted lever (see Fig. 1, right). The total added weight of the plasma actuation system was 700 grams, to produce a total weight of $W_{\text{tot}} = 2.88\ \text{kg}$.

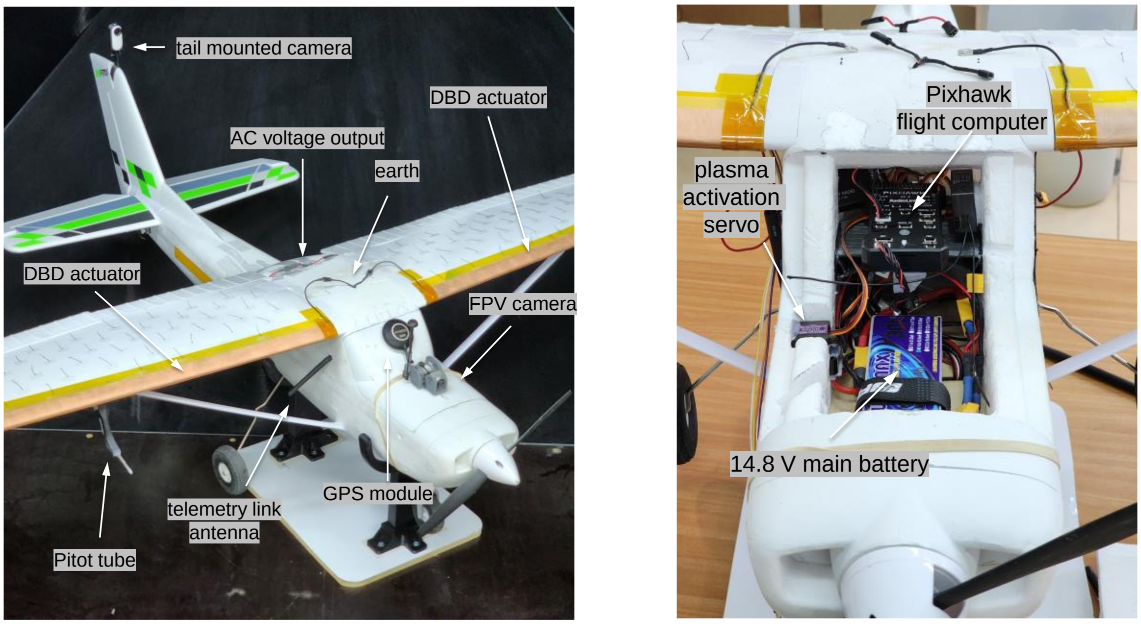


**Fig. 1. Photograph from above the nose region of the model with the front access hatch removed (shown on the left).**

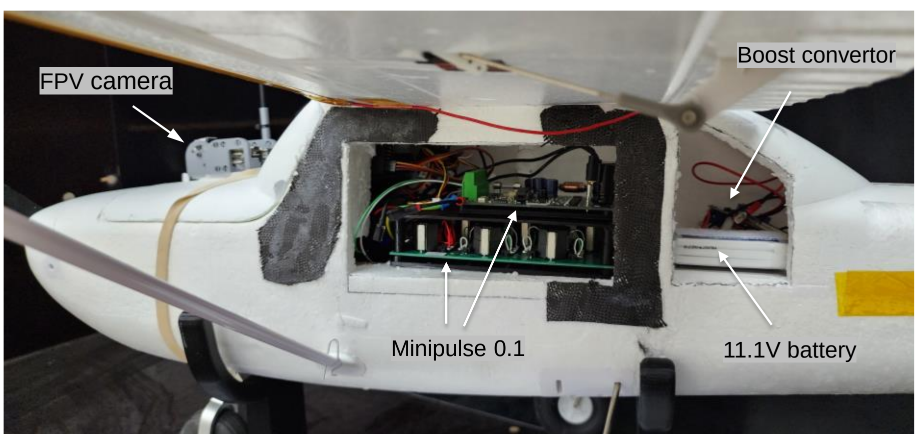


**Fig. 2. Photograph from the side of the model with the side access hatches removed.**

### B. Wind Tunnel Experiments

The identical model was used for both wind tunnel and flight experiments. The wind tunnel experiments were performed in an open-jet blow-down tunnel, where the original 1.0 × 0.61 m nozzle [30] was replaced with a 1.0 × 1.9 m nozzle. This new configuration has a maximum wind speed of $U = 16$ m/s, a maximum flow distortion of 2.5% and a maximum turbulence intensity of 0.5%. In addition to the model Pitot-tube, the wind tunnel speed was measured using a pitot-static probe, mounted upstream of the model, using a Siemens QBM3020-1U pressure transducer (±0.5 pascal total non-linearity) together with an E+E Elektronik EE211 humidity and temperature system. The landing gear was removed and its mounts were used to attach it to an aluminum sting with a six-component ATI Delta SI-330-30 balance (not shown). Load data were acquired for powered and unpowered conditions, with and without flaps deflected and with and without ailerons deflected. The pitch angle was recorded with a Singer Instruments Model MTS-D inclinometer, with a ±45° range and a ±0.009° non-linearity.

For selected experiments, tufts were attached to the wings (see Fig. 8) and each wing was filmed directly from above at 4 K resolution and 60 frames per second. Image processing was performed using the Adobe Photoshop smart object and stack mode features [31]. The images were imported as frames into Photoshop and, for each case, 200 consecutive frames were combined for analysis with the stack mode set to "Range". The Range stack mode takes the difference of the maximum and minimum non-transparent pixel values, resulting in an image that displays the movement of an object with high contrast to a non-moving element.

### C. Flight Experiments

Preliminary flight experiments were performed for under unpowered gliding with the actuators activated and then subsequently deactivated. Data logging and telemetry were performed using a Pixhawk flight computer (see Fig. 1, right) and tufts were filmed at 2.7 K resolution and 50 frames per second using an insta360 GO 2 camera positioned above the tail (see Fig. 1, left). The Pixhawk reads information from a radio receiver and commands the motors, servos, and other devices as needed. It also hosts a suite of sensors from accelerometers to compasses and is easily expanded to include multiple pressure sensors to be employed in future research. For all flight experiments, the open-source ArduPilot firmware was used in fly-by-wire_A mode. In this flight stabilization mode, it is not possible to roll beyond the preset limit (±45°) or pitch beyond the preset limits (±25°). All data were logged to an onboard SD card, in addition to a telemetry link between the vehicle and a ground station, and subsequently post-processed into a MATLAB format for analysis. A First-Person-View (FPV) system was also employed, with the camera mounted downstream of the propeller (see Fig. 1, left). For all flight experiments, $f_p = 118\text{Hz}$, $V_{\text{pp}} = 10.6\ \text{kV}$, $\text{d.c} = 9.5\%$, and $P_{pl} = 19\text{W}$.

## III. Discussion of Results

### A. Unpowered Model Wind Tunnel Experiments

Initial lift and drag coefficient data were acquired at $U = 10.0\ \text{m/s}$, in order to determine $C_{L,\max} = 1.40$ and thereby calculate $U_{\text{stall}} = 8.6\ \text{m/s}$, based on the total weight $W_{\text{tot}} = 2.88\ \text{kg}$ of the model. Hence the majority of unpowered experiments were performed at $U = 8.6\ \text{m/s}$, corresponding to $Re = 1.45 \times 10^5$, with supplemental experiments at $U = 10\ \text{m/s}$. Uncertainties in the balance measurements, in the lift and drag directions respectively, were ±210 and ±63 millinewtons, based on in-situ calibrations. These were significantly larger than the manufacture's balance resolution specifications of ±31 and ±16 millinewtons, respectively. At the $U = 8.6\ \text{m/s}$, the calibrated values corresponded to lift and drag coefficient uncertainties of $\Delta C_L \approx \pm 0.01$ and $\Delta C_L \approx \pm 0.003$, respectively. All wind tunnel data were acquired at 10,000 samples/second, for a minimum interval $(t_{\text{daq}})$ time corresponding to $t_{\text{daq}} U / \bar{c} = 200$. This ensure that the precision error, based on 95% uncertainty intervals, was always less than the calibration repeatability error.

Four different baseline (plasma not activated) configurations were tested, using combinations of the clean configuration (i.e., without tufts), with tufts, without the propeller installed and with the propeller windmilling. These data sets are presented as $C_L$ versus $\alpha$ (Fig. 3, left) and $C_L$ versus $C_D$ polar plots (Fig. 3, right), and the uncertainties described above are shown as error bars on the polar plot "no propeller, no tufts" data set. The combined tuft and windmilling propeller experiments were necessary because they corresponded to the *de facto* gliding flight experiments, described in section III.IV. Both lift and drag coefficient data showed very little variability between the different configurations. The windmilling propeller appears to reduce $C_{L,\max}$ slightly, by ~0.02, and reduce the stall angle $\alpha_s$ by approximately 1°, with or without tufts. The propeller also slightly increases the base drag coefficient.

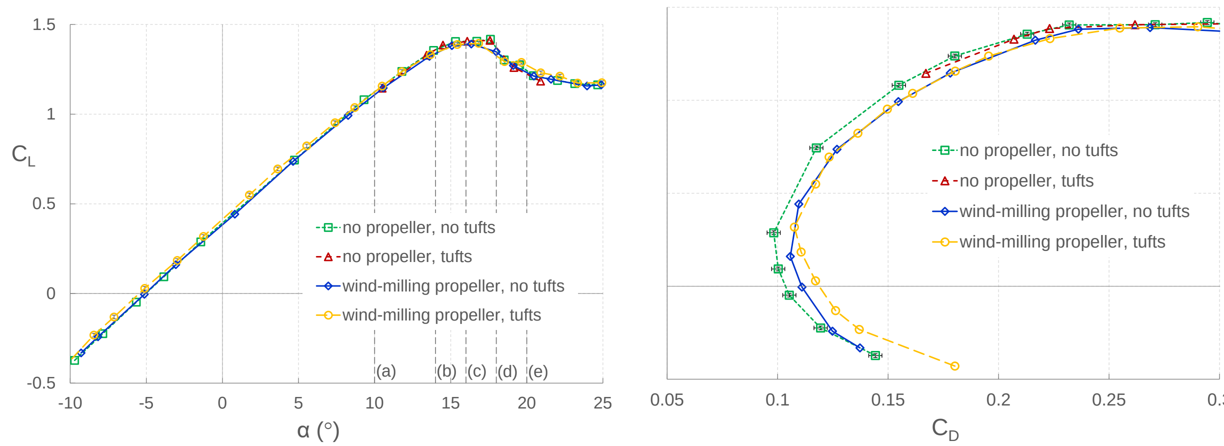


**Fig. 3. Lift and drag coefficients for four non-powered baseline (plasma not activated) experiments ($Re = 1.45 \times 10^5$). Flow visualization images in Fig. 4 correspond to angles indicated by (a)-(e).**

Processed tuft-based flow visualization (see section II.B) corresponding the angles indicated in Fig. 3 (left) are shown in Fig. 4, where the letters (a) to (e) identify the angles. At pre-stall angles, $\alpha = 10°$ and 14°, flow visualization images in (a) and (b), that show attached flow over the wings as expected. At $\alpha = 16°$ (c) there is a noticeable inboard trailing-edge separation close to the wings root on both wings, while the leading-edge flow remains attached. The right wing shows a larger separated region, which is most likely due to the wake shed by the pitot-static probe that is mounted at approximately at the mid-semi-span location and appears to exacerbate stall. At $\alpha = 18°$ (d) trailing-edge separation extends further upstream and outboard, particularly on the left wing. The stall behavior shown is desirable because the attached outboard flow ensures continued control authority of the ailerons. At $\alpha = 20°$ (e), separated flow extends over the entire right wing and most of the left wing.

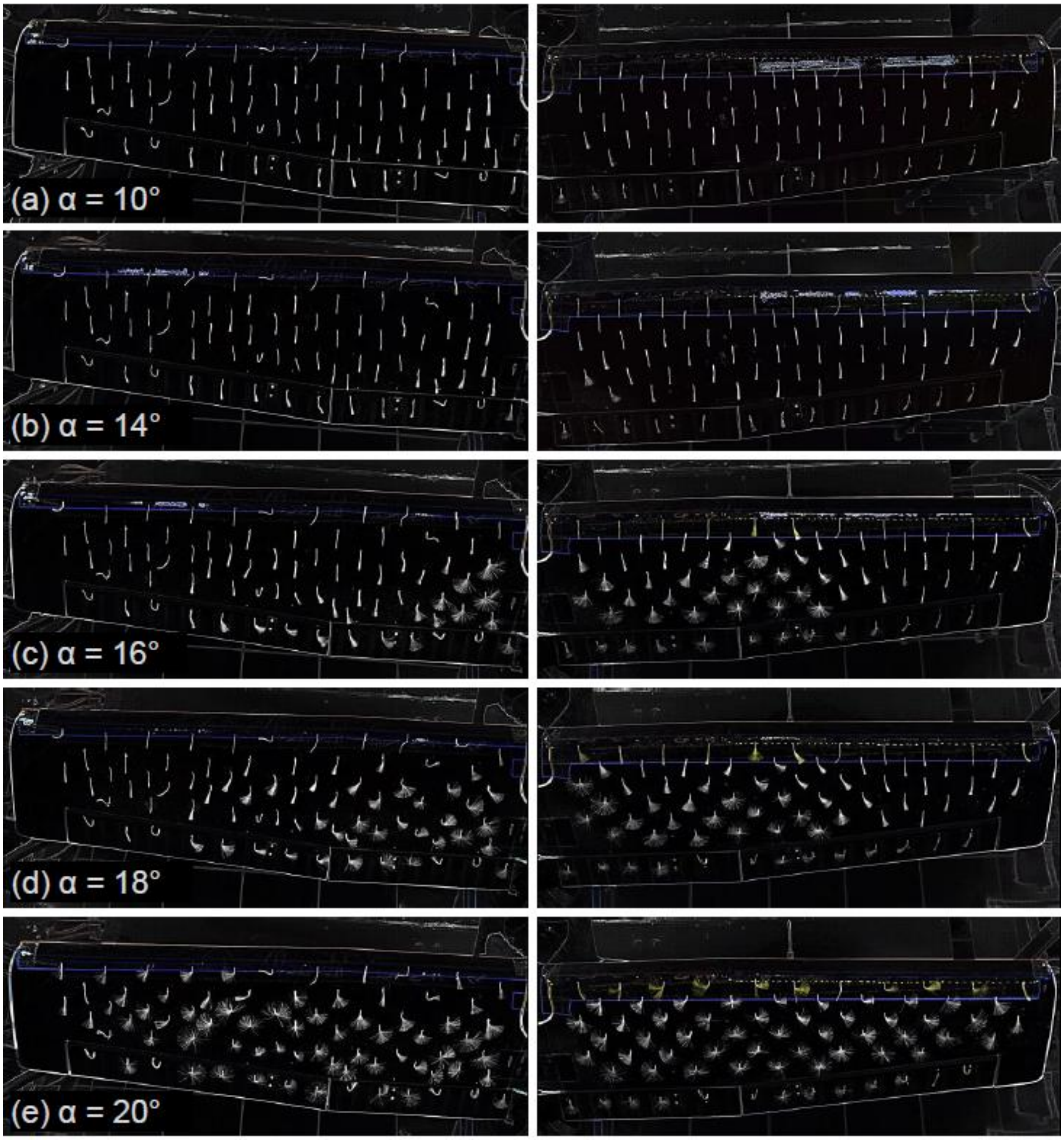


**Fig. 4. Processed tuft-based flow visualization with propeller windmilling: (a) to (e) correspond to the angles are indicated in Fig. 3.**

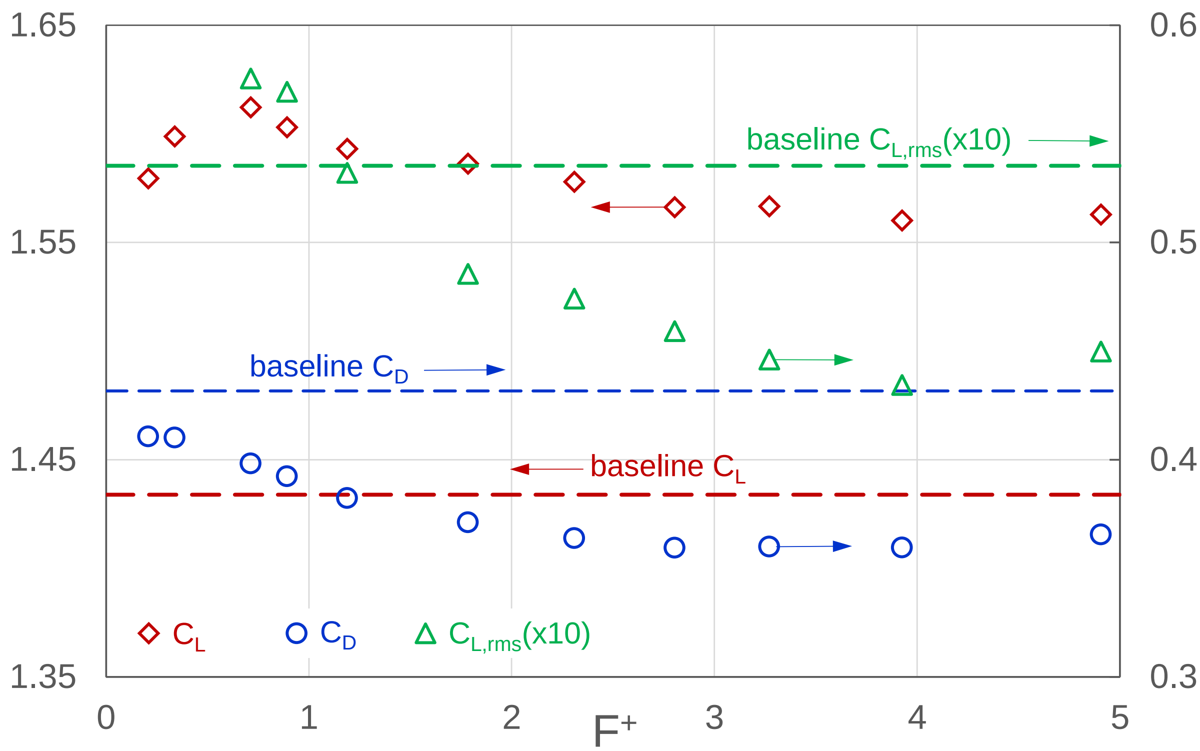


**Fig. 5. Model lift and drag coefficients as a function of reduced frequency at** $\alpha = 18°$ **and** $Re = 1.45 \times 10^5$.

The model was set at a post-stall angle of $\alpha = 18°$ and the aerodynamic response, as a function of pulsed plasma frequency at $V_{pp} = 11.0\ \text{kV}$, was determined. This involved the measurement of the aerodynamic forces while sequentially activating and deactivating the actuators at different pulsation frequencies $f_p$. At each condition, data were acquired for 10 seconds, corresponding to 340 convective time units. The lift and drag coefficient data are summarized as a function of the reduced frequency scan $F^+ \equiv f_p \bar{c} / U$ in Fig. 5, and the results are broadly consistent with the effects of actuation on airfoils [18,32]; namely a mild lift peak at $F^+ \approx 1$ and minimum drag in the approximate range $3 \le F^+ \le 4$. Relatively high levels of lift coefficient unsteadiness $(C_{L,\text{rms}})$ were recorded at the lower excitation frequencies. These were related to a flapping-mode resonance of the wings at approximately 26 Hz (corresponding to $F^+ = 0.8$), that was exacerbated by the wind tunnel setup. Therefore, although $0.7 \le F^+ \le 0.9$ produced the largest increase in the lift coefficient, the remainder of the wind tunnel experiments were performed at $F^+ = 3.5$

(corresponding to $f_p = 118$ Hz) and $\text{d.c.} = 12\%$, with a corresponding plasma input power $P_{pl} = 26$ W.

The effect of actuation on the lift and drag coefficients for angles of attack at, and beyond, stall is shown in Fig. 6, for the model without the propeller and with the propeller windmilling. In all instances, the effect of actuation on $C_{L,\max}$ is modest, between 0.02 and 0.03, although the overall $C_L$ changes are greater with the propeller windmilling. A welcome result is that for each configuration, the post-stall $C_L$ never drops below $C_{L,\max}$ and this implies that the model can fly safely at angles well exceeding the nominal baseline static stall angle. The relatively small effects on $C_{L,\max}$ are due to both the non-optimum reduced frequency employed and the fact that the excitation effects are not uniform along the span (see flow visualization below), in contrast to the observations made on two-dimensional airfoils. Similar clean wing, propeller windmilling experiments were performed at on the $U = 12$ m/s (corresponding to $Re = 2.03\times10^5$, not shown) with similar effects to those presented in Fig. 6.

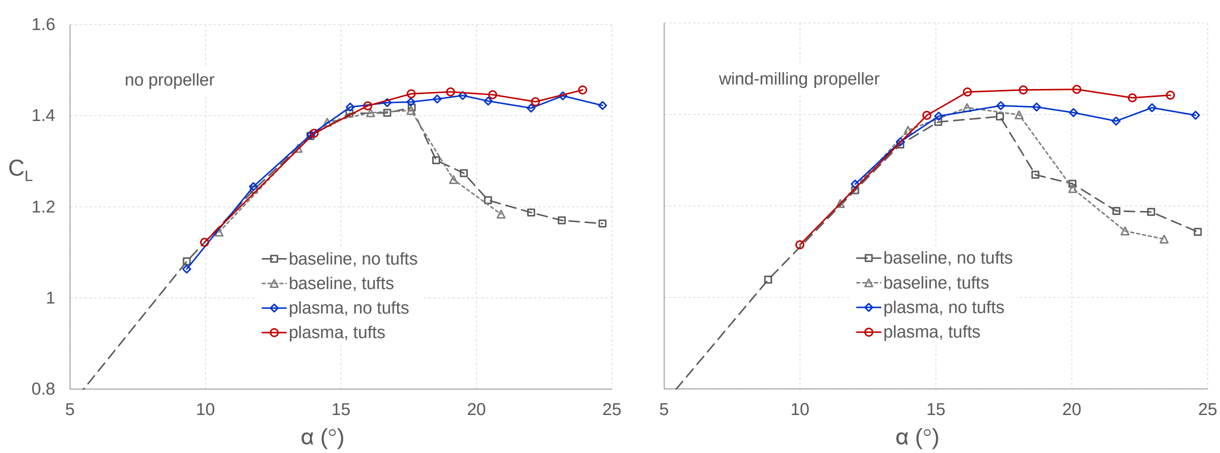


**Fig. 6. Effect of actuation on lift coefficient for configurations with and without the propeller installed** $(Re = 1.45\times10^5)$**.**

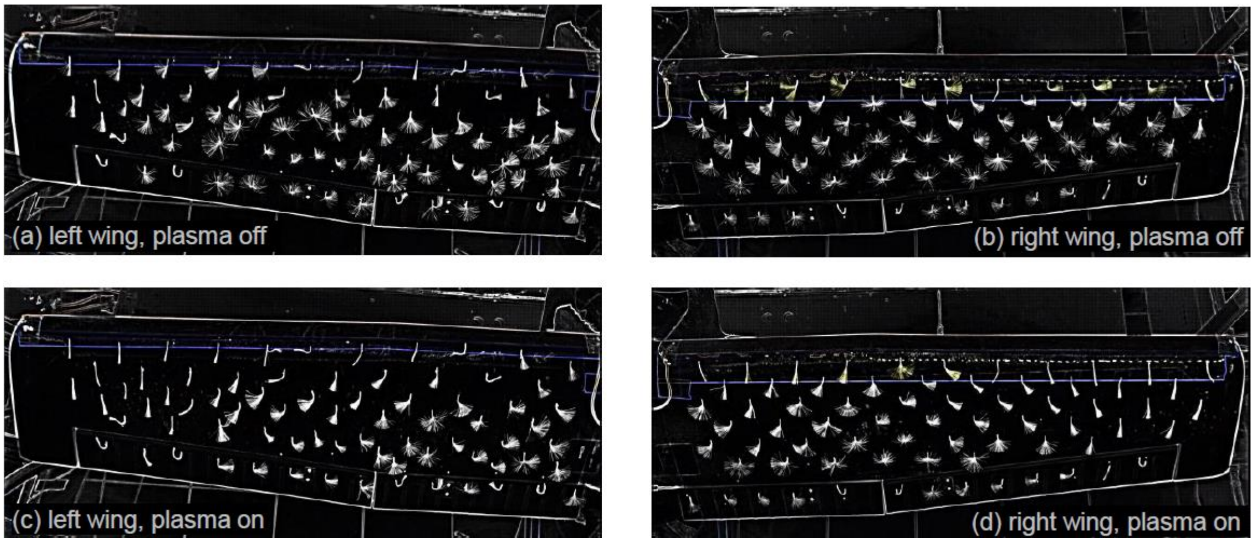


**Fig. 7. Processed tuft-based flow visualization for baseline and actuated conditions with the propeller windmilling at** $\alpha = 20°$ and $Re = 1.45 \times 10^5$**.**

Processed tuft-based flow visualization images corresponding to baseline and actuated cases at $\alpha = 20°$ are shown for both wings in Fig. 7. On the basis of the direction and amplitude of the tuft-fluctuations, it is clear that large-scale separation is present on both wings under baseline conditions (see Fig. 7a and Fig. 7c), with the exception of the left wing tip region. One possible reason for the asymmetry is that the clockwise windmilling propeller produces a counter-clockwise wake, resulting in upwash and downwash upstream of the right and left wings respectively. Another possible reason for the asymmetry is the Pitot tube mounted below the right wing that produces a wake that interacts with the wing at high angles of attack. When actuation is applied (see Fig. 7b and Fig. 7d), the predominant effect is observed on the outboard parts of the wing, whose spanwise regions corresponds to the aileron locations. In fact, the outer one-third of the span is fully attached. This observation is consistent with flow control applied near wing-tips, where flow attachment is enhanced by entrainment of flow over the wingtip region [33-37]. Inboard, however, the effect is observed mainly closer to the leading-edge—indicating that leading-edge stall is prevented—and full boundary layer attachment is not attained. The lack of complete attachment of the boundary layer across the span is consistent with the modest $C_{L,\max}$ increases shown in Fig. 6b.

The effect of actuation, with simultaneous deflection of inboard flaps $(\delta = 45°)$ commonly deployed during take-off and landing, is shown in Fig. 8. Despite the relatively large flap deflections, the increases in $C_L$ are relatively small because the flap only covers 38% of the span. The actuation results are qualitatively similar to the undeflected flaps case, in the sense that only modest increases in $C_{L,\max}$ are observed while post-stall $C_L$ never drops below the baseline $C_{L,\max}$. The maintenance of post-stall $C_L$ by the prevention of leading-edge stall may be exploited to reduce takeoff and landing roll, by reducing the common safety margin $U_{\min} = 1.2U_{\text{stall}}$ [1].

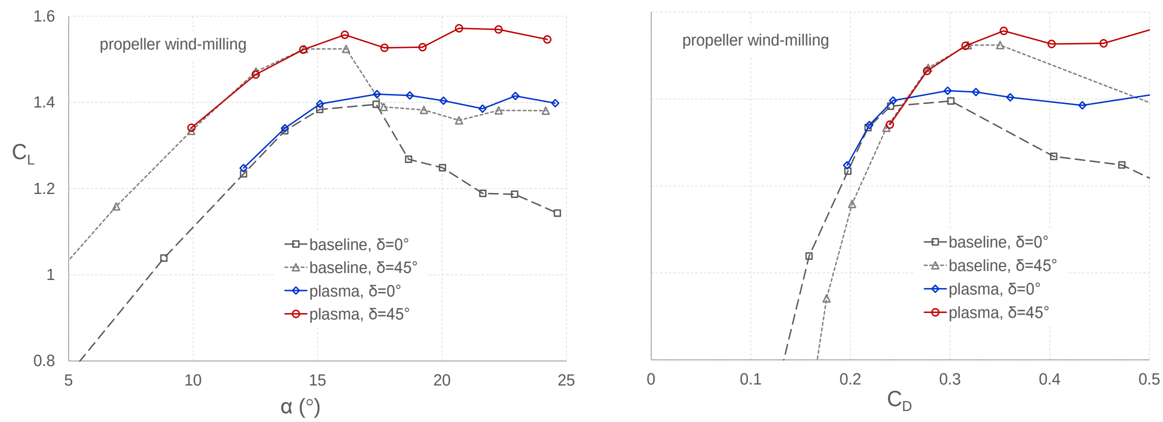


**Fig. 8. Effect of actuation on lift and drag coefficients with flap deflection, where the propeller is installed** $(Re = 1.45\times10^5)$.

### B. Powered Model Wind Tunnel Results

At present, very little is known about the effectiveness of plasma actuators mounted aft of a propeller. To investigate this, powered wind tunnel experiments were performed for the baseline and actuated cases in the following manner. A wind speed $U > U_{\text{stall}}$ was selected and the corresponding $C_L$ was calculated based on the weight of the model. The model was then set to an angle-of-attack, determined from Fig. 6, and power was supplied to the propeller. The propeller input power and angle-of-attack were then serially and iteratively varied until both the lift and drag were balanced, i.e., readings of zero to within ±0.15 N for lift and drag (i.e., a null balance reading). This procedure was repeated for successively reduced wind speeds and the results of the recorded motor power $P$ as a function of wind speed are shown in Fig. 9. Input power for $U > 9$ m/s showed no difference between baseline actuated cases, owing to the fact that separation was not present on the wings. However, as the stall speed was approached, a power saving was observed, with a reduction of between 16 W and 36 W at $U = 8.75$ m/s, depending on the angle-of-attack.

This compared favorably to the gross plasma system input power of 26 W. For wind speeds $U < 8.75\text{m/s}$, zero balance readings of the baseline lift component could not be attained. With actuation, however, zero balance readings were obtained at $U = 8.25$ m/s at $\alpha = 20°$, which corresponds to a 6% decrease in $U_{\text{stall}}$. This result was surprising because it corresponds to a 12% increase in $C_{L,\max}$, which is far greater than the maximum attained during unpowered experiments, namely $\Delta C_{L,\max} < 3.6\%$ (see Fig. 6).

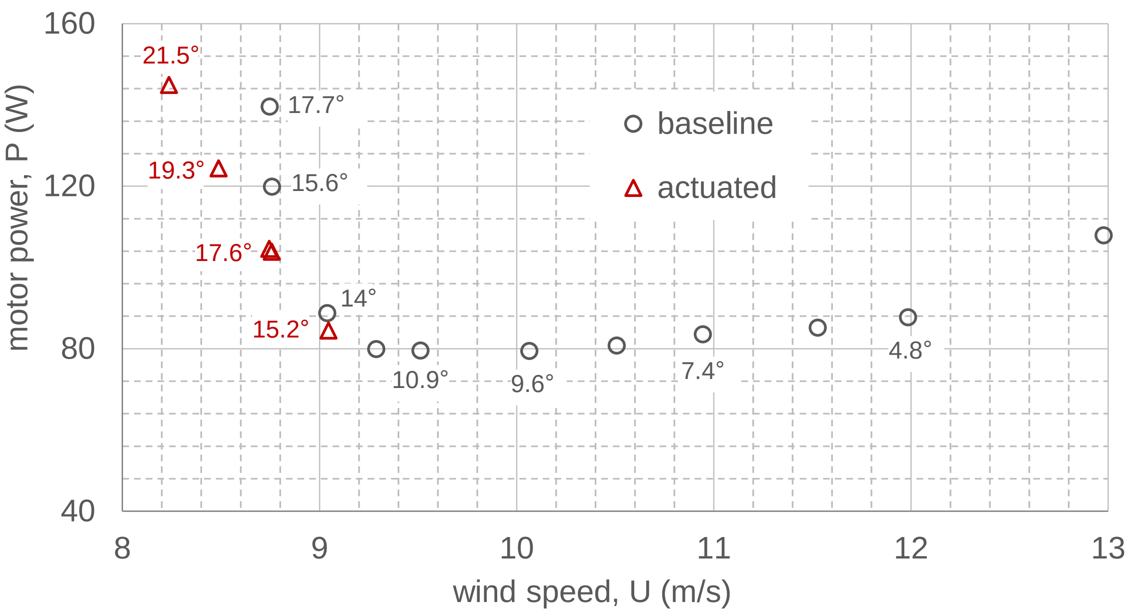


**Fig. 9. Input motor power as a function of wind tunnel speed for powered wind tunnel experiments. Corresponding angle-of-attack labels are also shown.**

The likely reason for the stall speed observations in Fig. 9 can be extracted from the powered flow visualization images shown in Fig. 10, together with a comparison to the unpowered model images shown in Fig. 7. For the baseline, powered versus unpowered cases (Fig. 7a,b versus Fig. 10a,b), the left and right wings are affected differently, possibly due to the clockwise propeller rotation. On the left wing the powered prop-wash promotes separation inboard, but simultaneously promotes attachment over approximately one-third of the outboard span. This can most clearly be seen by comparing the tip region and the first line of tufts downstream of the actuator in Fig. 7a and Fig. 10a. On the right wing, the prop-wash promotes separation over almost the entire span, with the exception of the region very close to the tip. This observation is not consistent with our explanation based on the expectation of downwash upstream of the right wing. For angles of attack

$\alpha \leq 16°$ this phenomenon was not observed and only manifests at post-stall angles of attack. The promotion of inboard separation may also be exacerbated by the propeller shaft angle, which is deflected at 8° downwards from the fuselage. With actuation, the prop-induced separation is significantly ameliorated most notably over the entire right wing (see Fig. 10d) and mainly near the leading-edge of the left wing (see Fig. 10c). It thus appears that the difference in stall speed observed in Fig. 9 is due to control of the separation that is exacerbated by the prop-wash at post-stall angles of attack.

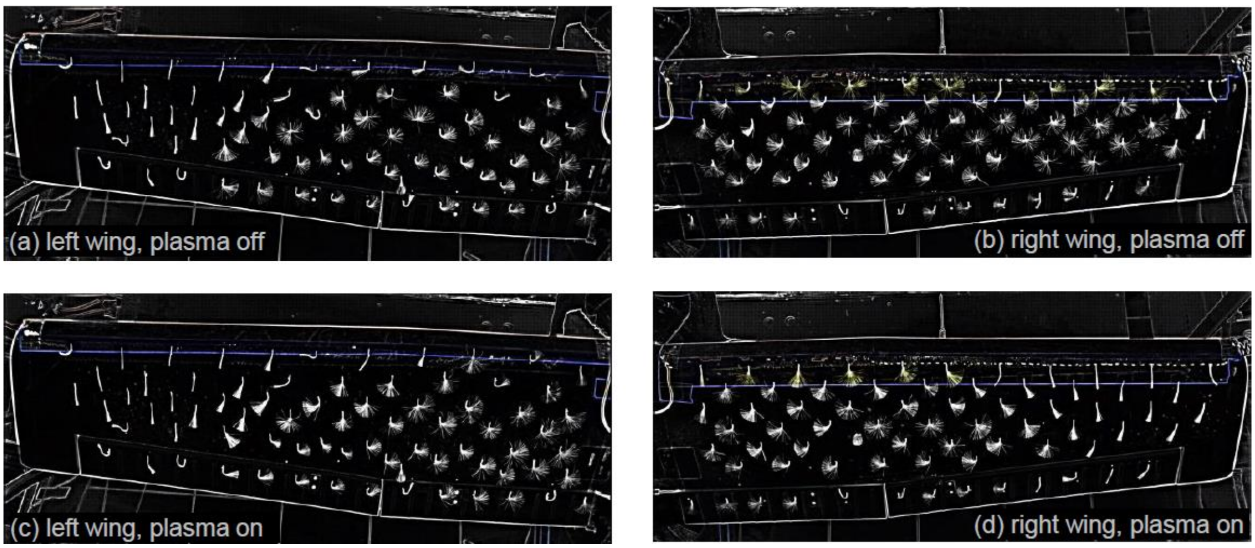


**Fig. 10. Processed tuft-based flow visualization for powered wind tunnel experiments at $\alpha = 20°$.**

## IV. Unpowered Flight Experiments

Flight experiments were conducted in order to quantify the flight characteristics with and without the actuators operational. For the purpose of eliminating the effects of propwash, the experiments reported here were performed during unpowered gliding with the propeller windmilling. Selected Pixhawk flight data and control surface deflections are shown for a representative experiment in Fig. 11, with reference to an arbitrary time $t_0$, such that $t' = t - t_0$. These experiments were performed with the ArduPilot flight controller set in the fly-by-wire_A mode.

The aeroelasticity of the tail and wings prevented the aircraft from remaining acceptably centered in the field of view to perform the image stacking, like those performed in the wind tunnel experiments. Therefore, a motion tracking profile was generated using Adobe After Effects [36]. This allowed for each of the video frames to be transformed (translation and rotation) to center the aircraft in the field of view based on tracking points, that were selected in high contrast regions on the root of the wings, near the fuselage. Once centered, a static mask was applied to regions around the aircraft to reduce the background movement noise and the image stacking method was applied as before. The flight experiment image stacks included ±10 frames, corresponding to ±200ms time windows, centered at five representative times shown in Fig. 12a to Fig. 12f. The representative times shown in the figure are indicated by the letters (a) to (f) at the top of Fig. 11.

The experiment begins with a climb to approximately 50 meters, with the plasma actuators activated, whereafter the motor power is shut off, at $t' \approx 7\text{s}$. Without power the model immediately begins to lose altitude and flight speed. The pitch angle does not drop significantly below 0° and the tufts indicate that the flow over both wings is nominally attached (Fig. 12a). The flight controller increasingly deflects the elevator upwards to keep the nose up. The model reaches its stall speed at $t' \approx 14.3\text{s}$, where a small region of separated flow can be seen inboard on the right wing, with some spanwise flow inboard on the left wing (Fig. 12b). Note that a certain amount of image smearing occurs due to the variations in tuft locations within the 400ms time-windows. At $t' = 14.7\text{s}$, the actuators are deactivated and shortly afterwards $(t' \approx 15.0\text{ s})$ large-scale separation is visible, mainly on the inboard part of the right wing (Fig. 12c). The resulting loss of lift on the right wing produces a sharp 28° roll to the right, a –8° pitch down and a 31° right-heading change at $t' \approx 16.3\text{s}$ (i.e., 1.6 seconds after deactivation; see Fig. 12d). These changes occur despite the hard-left rudder deflection and left aileron deflections introduced by the flight controller, where the latter is visible in Fig. 12d. The separated flow over the right wing recovers at $t' \approx 17\text{s}$, when the model rolls rapidly to the left, and this is accompanied by stall of the left wing (see Fig. 12e). To compensate, the controller switches the direction of the aileron and rudder at $t' \approx 17.3\text{s}$ and the large roll to the left results in flow separation inboard on the left wing (Fig. 12f). Following this, the controller struggles to maintain control until $t' \approx 25\text{s}$, when the pilot is compelled to increase thrust due to the rapid loss of altitude.

The main takeaway from this experiment, and others like it not shown here, is that plasma actuators facilitate stable flight near $U_{\text{stall}}$, in contrast to the baseline case. This is seen by: (a) the uncontrolled and rapid pitch, roll and yaw, and rapid loss of altitude due to massive separation when the actuators are shut off; and (b) the large control surface deflections required in an attempt to maintain stable flight.

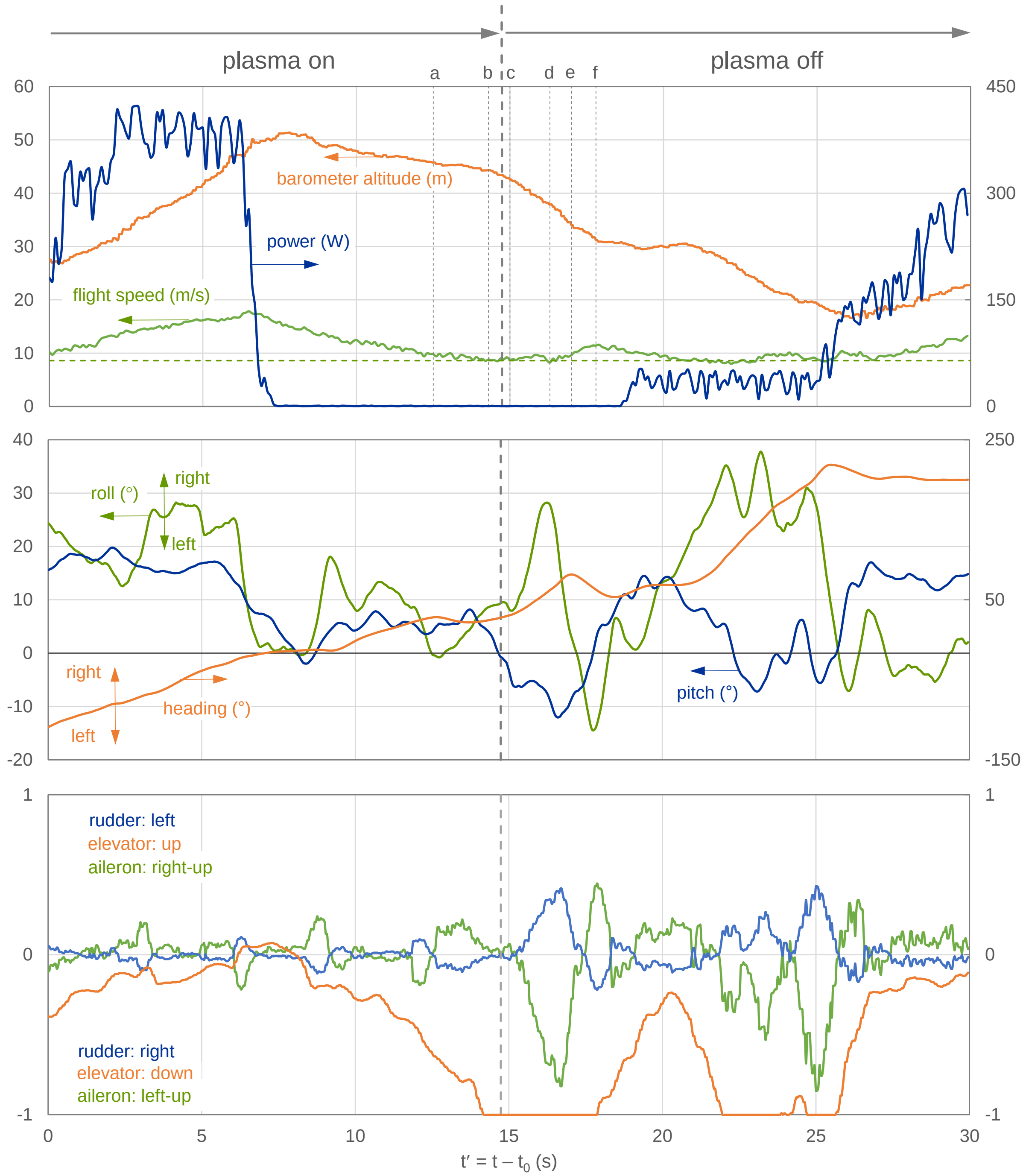


**Fig. 11. Flight data and control surface deflection data for a gliding flight experiment, with the propeller windmilling.**

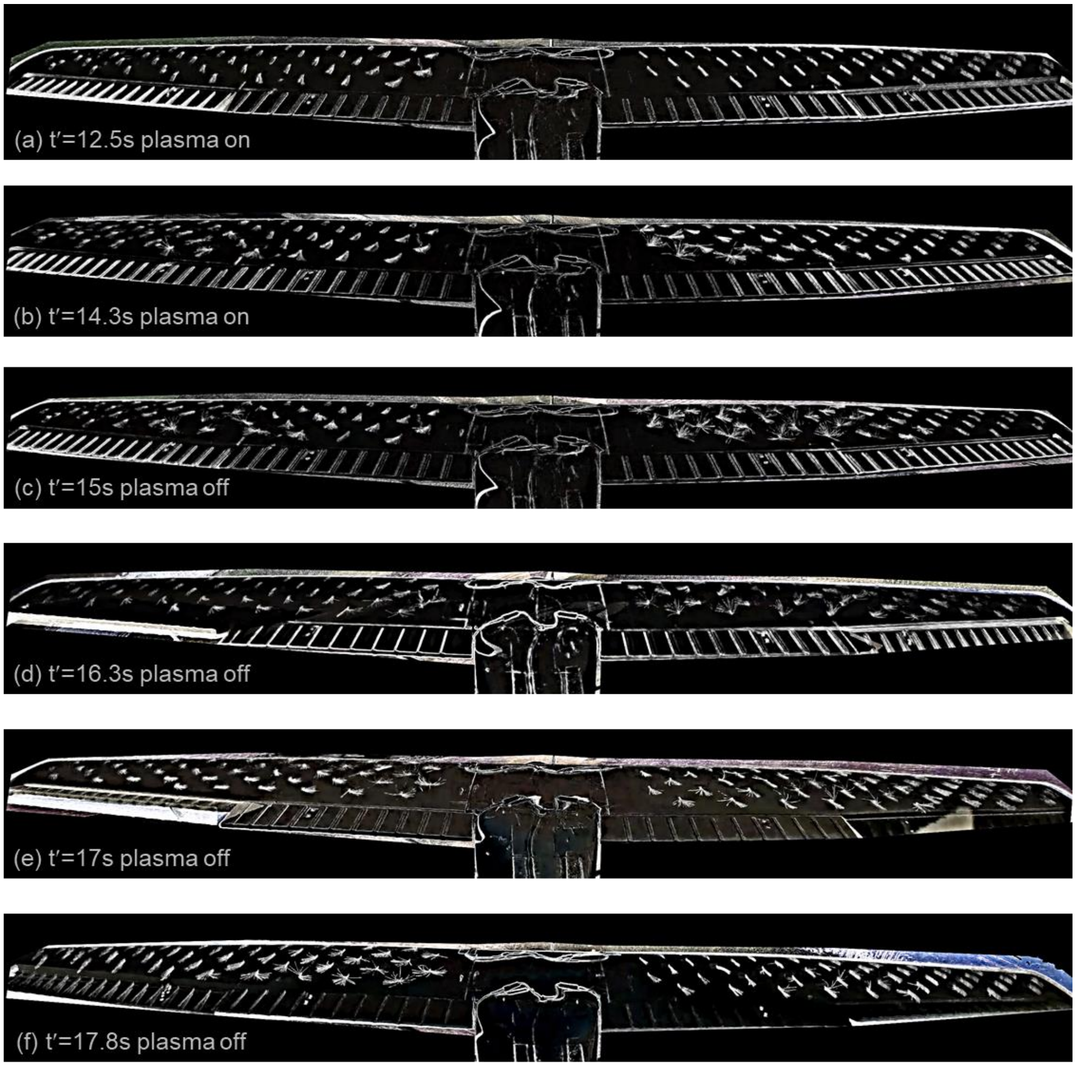


**Fig. 12. Processed tuft flow visualization images extracted from the tail-mounted video camera prior to and following deactivation of the actuators at $t' = 14.7\text{s}$.**

## V. Full-Scale Aircraft Implementation

The DBD plasma-based stall-control system described here should be evaluated on a full-scale GA aircraft. Using the Cessna 172 as an example, the actuators can either be retrofitted to the wings, as described here, or incorporated into the wing geometry during the design stage. An initial evaluation should be made using a full-scale Cessna-modified NACA 2412 airfoil at full-scale stall speeds—and therefore Reynolds numbers—where DBD plasma specifications need to account for stall speed and scale differences. Furthermore, because plasma actuators are only required for stall control, they are not pulsed continuously, and are only required when the aircraft nears stall. Therefore, a strategy for automatic (closed-loop) control must also be developed.

## A. DBD Plasma Actuator Requirements

For the full-scale (f.s.) aircraft, the body force ( $F_B'$, thrust per unit span) of the plasma actuator must scale with the momentum coefficient $C_\mu \equiv F_B' / qc$ , i.e., $F_B'$ must be increased by the ratio $(qc)_{\text{f.s.}} / (qc)_{\text{model}}$ [12]. For the experiments described in section III.A, the maximum wind speed for which actuation was effective was 10.0 m/s. However, the minimum $C_\mu$ required to maintain control authority, which is determined by reducing $V_{\text{pp}}$, was not determined. Therefore, the estimates presented below are conservative.

Based on the full-scale stall speed of 47 knots [38] and a chord ratio of 6.1:1 the body force must be increased by a factor 36. This cannot be achieved with the Minipuls 0.1, whose maximum $V_{\text{pp}} = 12$ kV, and we therefore consider body forces achievable by higher power high-voltage generators. Body force calibrations of actuators (d.c.=100%) with thicker dielectrics (1 mm and 3 mm silicone rubber) and higher power high-voltage generators of the same family (namely, Minipuls 2® and Minipuls 4®, weighing 1.2 and 4.5 kg, respectively), were performed and compared to the 0.4 mm dielectric actuator used here (see Fig. 3, adapted from [17]). The ratio between the highest body force (3 mm dielectric, Minipuls 4) and current actuator (0.4 mm dielectric) was 21. This ratio somewhat less than our conservative estimate of 36. Nevertheless, even larger body forces can be attained in three ways: either using a thicker dielectric; a more powerful generator (for example, the Minipuls 6®); or both. In terms of weight, the Minipuls 6 is viable for this application with a total weight of 8.7 kg, which is less than 1% of the aircraft gross weight ($1.11\times10^3$ kg). An alternative is to drive the actuators with pulsed-DC waveforms, where voltage pulse-widths are typically either $\mathcal{O}(10^1)$ to $\mathcal{O}(10^2)$ [39], or $\mathcal{O}(10^1)$ ns [16,40]. In the former case, the body forces generated are more than an order-of-magnitude greater than those produced by AC waveforms. In the latter case, gas velocities are negligible, but rapid $\mathcal{O}(10^0)$ µs heating and the resultant pressure increases produce shock waves, that are effective for separation control under compressible conditions [16,41].

The combination of higher stalling speed and increased dimensions also increases the stalling Reynolds number by a factor of 16 to $2.4\times10^6$. This is likely a secondary consideration, because it was shown by [16] that increasing the Reynolds number from $0.56\times10^6$ to $2.26\times10^6$ does not degrade the aerodynamic effectiveness of the DBD plasma actuators. Furthermore, in the full-scale application the flow can still be considered incompressible, because the Mach number remains below 0.1.

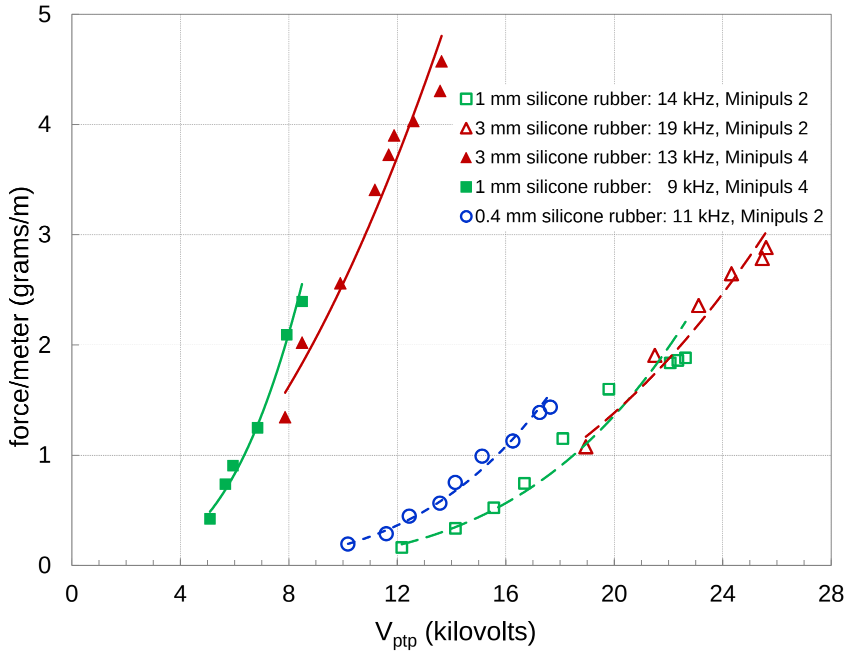


**Fig. 13. Body force calibration of DBD plasma actuators as a function of peak-to-peak voltage (d.c.=100%), with least-squares power-law curves, for different dielectric thicknesses and different Minipuls® technology high-voltage generators (adapted from [17]).**

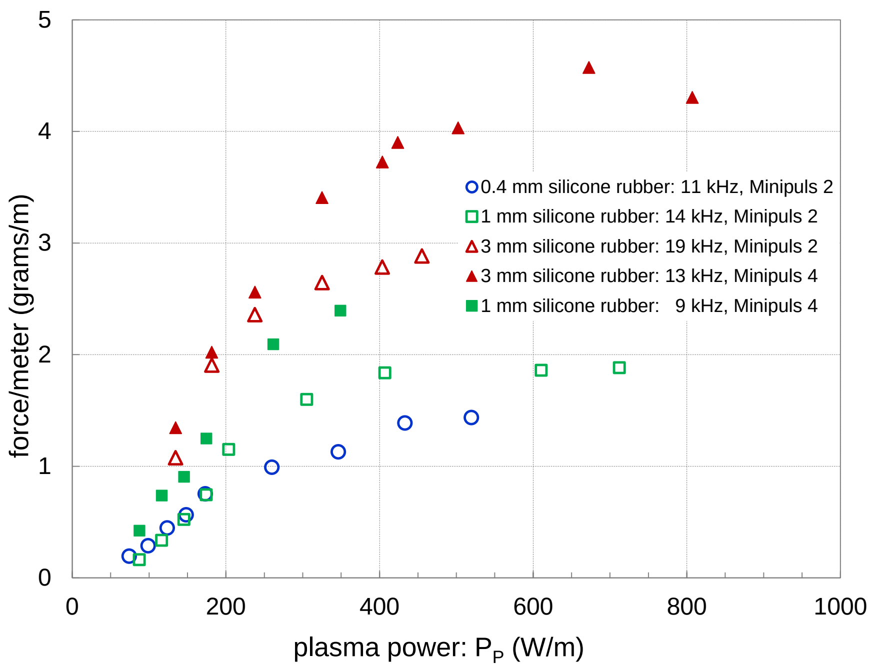


**Fig. 14. Body force calibration of DBD plasma actuators as a function of gross (direct current: DC) input power (duty cycle: d.c. =100%) corresponding to the data in Fig. 13.**

The power required to drive the actuators can be estimated from Fig. 14, which represents the gross DC power supplied to the high-voltage generators at d.c.=100%. For full-scale estimates, we assume that the power consumed is 1-kilowatt/meter and that d.c.=12.5% as in the wind tunnel experiments. This value is also conservative, i.e., high, because the minimum d.c. required to maintain control authority was not determined. Using this value, and the full-scale wingspan of 11 meters [38], the gross DC power required to drive the actuators is approximately 1.4 kilowatts, that can easily be achieved with a lithium-ion battery.

**B. Automatic Control**

For purposes of full-scale implementation, DBD plasma actuators should not be pulsed continuously; rather, they should only be initiated when the aircraft is at, or close to, stall. Hence, at least one sensor must be deployed, within a closed-loop control system, to provide feedback for initiation and termination, as necessary [42]. A simple way to implement closed-loop control is to employ the existing stall-control system on the aircraft. As the aircraft approaches stall, the stagnation point crosses over an orifice (the scoop), and the resulting negative air pressure sucks air through a reed, producing an audible warning. This system can be adapted to initiate and terminate actuation as necessary. We evaluated such a system using a semi-span wing from the model used in this investigation, that was based on zero-crossings of a pressure sensor just below the leading-edge—in the location of the scoop orifice—to either initiate or terminate plasma pulsations [43]. Lift and drag coefficient results, based on closed-loop control, were compared with open-loop (continuous) plasma pulsations under static and dynamic―harmonic and pitch-and-hold―angle-of-attack variations. Under all light, moderate and deep stall scenarios, at a wide range of reduced frequencies, negligible differences were observed between open- and closed-loop control, thereby demonstrating the viability of the closed-loop system. With increasing pitchrate, the angles-of-attack corresponding to pitch-down zero-crossings increased successively, to angles greater than the static stall angle. This had no measurable effect on the results because the timescales governing boundary layer separation were at least an order-of-magnitude larger than the time-intervals between the zero-crossing angle and the static stall angle. Such as system can easily be retrofitted to any general aviation aircraft that incorporates scoop-type stall warning systems.

# VI. Conclusions

Wind tunnel and flight experiments were performed on a battery-powered FMS Ranger PNP RC model, where pulse-modulated plasma actuators were deployed along the wing's leading edges for the purpose of controlling stall. Wind tunnel experiments showed that the effect of a windmilling propeller and tufts, that were subsequently present during flight experiments, had only a minor effect on stall. Post-stall pulsed plasma frequency scans showed that reduced frequencies of approximately 3.5 were effective for controlling stall and minimizing lift amplitude vibrations. Actuation on the unpowered model, with and without the windmilling propeller present, resulted in modest maximum lift coefficient increases. Nevertheless, under actuation, post-stall lift coefficients never dropped below the baseline (non-actuated) maximum lift coefficient, up to 8° (the maximum tested) beyond the static stall angle. This was also the case when the inboard flaps were deflected to 45°. Tuft-based flow visualization showed that the predominant effect of the plasma actuators was outboard near the tips, where the flow was fully attached, with the prevention of leading-edge stall inboard. Powered wind tunnel tests showed that the propeller wake exacerbates separation at post-stall angles of attack, but these effects are partially overcome by plasma actuation that prevents leading-edge stall and results in a 6% decrease in stall speed. As in the unpowered experiments, the outboard flow is fully attached by actuation.

Preliminary flight experiments were conducted during unpowered gliding with the propeller windmilling, where data logging and telemetry were performed using a Pixhawk flight computer, in a flight stabilization mode, while tufts were filmed by a tail-mounted camera. The experiments were performed by gliding close to the stall speed with the actuators activated, and subsequently deactivated. Following deactivation, large-scale separation was observed on the right wing resulting in large rolling, pitching and yawing amplitudes, accompanied by a dramatic loss in altitude.

A DBD plasma-based stall-control system can be implemented on a full-scale GA aircraft, providing the full-scale stall speeds, corresponding Reynolds number and increased geometry are counted for. Furthermore, an automatic closed-loop scheme can easily be implemented by adapting the stall warning system on the aircraft to either initiate or terminate actuation as necessary.

## References


1. Anderson, J.D., "Introduction to Flight," 8th Edition, McGraw-Hill Education, New York, 2006, pp. 522-530.
2. Ellis, D.R. and Steinberger, J., "A study of lightplane stall avoidance and suppression," Report No. FAA-RD-77-25, Department of Transportation, Federal Aviation Administration, System Research & Development Service, 1977. https://apps.dtic.mil/sti/pdfs/ADA039223.pdf.
3. Kenny, D.J., "Stall and spin accidents: Keep the wings flying," AOPA Air Safety Institute, Publisher: Richard G. McSpadden, Jr., Frederick, MD, 2017. https://www.aopa.org/-/media/files/aopa/home/pilot-resources/safety-and-proficiency/accident-analysis/special-reports/stall_spin.pdf
4. Fala, N., "An analysis of fixed-wing stall-type accidents in the United States," *Aerospace*, Vol. 9, No. 4, 2022, p. 178. https://doi.org/10.3390/aerospace9040178.
5. Torenbeek, E., "An introduction to wing design. In: Synthesis of subsonic airplane design," Springer, Dordrecht, 1982. https://doi.org/10.1007/978-94-017-3202-4_7.
6. Lin, J.C., "Review of research on low-profile vortex generators to control boundary-layer separation," *Progress in Aerospace Sciences*, Vol. 38, Issues 4-5, 2002, pp. 389-420. https://doi.org/10.1016/S0376-0421(02)00010-6.
7. Fouatih, O.M., Imine, B. and Medale, M., "Numerical/experimental investigations on reducing drag penalty of passive vortex generators on a NACA 4415 airfoil," *Wind Energy*, Vol. 22, No. 7, pp. 1003-1017. https://doi.org/10.1002/we.2330.
8. Quackenbush, T., McKillip, R. and Whitehouse, G., "Development and testing of deployable vortex generators using SMA actuation," 28th AIAA Applied Aerodynamics Conference, p. 4686, 2010. https://doi.org/10.2514/6.2010-4686.
9. Nissle, S., Kaiser, M., Hübler, M., Gurka, M. and Breuer, U., "Adaptive vortex generators based on active hybrid composites: from idea to flight test," *CEAS Aeronautical Journal*, Vol. 9, 2018, pp. 661-670. https://doi.org/10.1007/s13272-018-0316-1.
10. Morice, S.D., Ginnell, K., Geary, S., Baughn, J. and Robinson, S.K., "Detection of boundary layer separation and implementation of autonomous vortex generators," AIAA Paper No. 2020-0788, Scitech 2020 Forum, 6-10 January 2020, Orlando, FL. https://doi.org/10.2514/6.2020-0788.

11. Müller-Vahl, H., Nayeri, C.N., Paschereit, C.O. and Greenblatt, D., "Dynamic stall control via adaptive blowing," *Renewable Energy*, Vol. 97, 2016, pp. 47-64. https://doi.org/10.1016/j.renene.2016.05.053.
12. Greenblatt, D. and Wygnanski, I., "The control of separation by periodic excitation," *Progress in Aerospace Sciences*, Volume 36, Issue 7, 2000, pp. 487-545. https://doi.org/10.1016/S0376-0421(00)00008-7.
13. Hansen, L. and Bons, J., "Flow Measurements of vortex generator jets in separating boundary layer," *Journal of Propulsion and Power*, Vol. 22, No. 3, 2006, pp. 558-566. https://doi.org/10.2514/1.13820.
14. Corke, T.C., Post, M.L., and Orlov, D.M., "SDBD plasma enhanced aerodynamics: concepts, optimization and applications," *Progress in Aerospace Sciences*, Vol. 43, 2007, pp. 193-217. https://doi.org/10.1016/j.paerosci.2007.06.001.
15. Cattafesta III, L.N. and Sheplak, M., "Actuators for active flow control," Annual Review of Fluid Mechanics, Vol. 43, No. 1, 2011, pp. 247-272. https://doi.org/10.1146/annurev-fluid-122109-160634.
16. Kelley, C. L., Bowles, P. O., Cooney, J., He, C., Corke, T. C., Osborne, B. A., Silkey, J. S., and Zehnle, J., "Leading-Edge Separation Control Using Alternating-Current and Nanosecond-Pulse Plasma Actuators," *AIAA Journal*, Vol. 52, No. 9, 2014, pp. 1871-884. https://doi.org/10.2514/1.J052708.
17. Keisar, D., Hasin, D. and Greenblatt, D., "Plasma actuator application on a full-scale aircraft tail," *AIAA Journal*, Vol. 57, No. 2, 2019, pp. 616-627. http://dx.doi.org/10.2514/1.J057233.
18. Greenblatt, D., Göksel, B., Rechenberg, I., Schüle, C., Romann, D. and Paschereit, C.O., "Dielectric barrier discharge flow control at very low flight Reynolds numbers," AIAA Journal, Vol. 46, No. 6, 2008, pp. 1528-1541. https://doi.org/10.2514/1.33388.
19. De Troyer, T., Hasin, D., Keisar, D., Santra, S. and Greenblatt, D., "Plasma-based dynamic stall control and modelling on an aspect-ratio-one wing," *AIAA Journal* Vol. 60, No. 5, 2022, pp. 2905-2915. https://doi.org/10.2514/1.J060933.
20. Sidorenko, A., Budovsky, A., Pushkarev, A. and Maslov, A., "Flight testing of DBD plasma separation control system," AIAA Paper No. 2008-373, 46$^{th}$ AIAA Aerospace Sciences Meeting and Exhibit, 7-10 January 2008, Reno, NV. https://doi.org/10.2514/6.2008-373.

21. Grundmann, S., Frey, M. and Tropea, C., "Unmanned aerial vehicle (UAV) with plasma actuators for separation control," AIAA Paper No. 2009-698, 47th AIAA Aerospace Sciences Meeting including The New Horizons Forum and Aerospace Exposition, 5-8 January 2009, Orlando FL. https://doi.org/10.2514/6.2009-698.
22. Friedrichs, W., "Unmanned Aerial Vehicle for Flow Control Experiments with Dielectric Barrier Discharge Plasma Actuators," PhD Thesis, Technische Universität Darmstadt, 2014. https://tuprints.ulb.tu-darmstadt.de/id/eprint/3776.
23. Su, Z., Li, J., Liang, H., Zheng, B.R., Wei, B., Chen, J. and Xie, L.K., "UAV flight test of plasma slats and ailerons with microsecond dielectric barrier discharge," Chinese Physics B, Vol. 27, No. 10, 2018, 105205. https://doi.org/10.1088/1674-1056/27/10/105205.
24. Sekimoto, S., Kato, H., Fujii, K. and Yoneda, H., "In-Flight Demonstration of Stall Improvement Using a Plasma Actuator for a Small Unmanned Aerial Vehicle," Aerospace, Vol. 9, No. 144 (18 pages), 2022. https://doi.org/10.3390/aerospace9030144.
25. Fratello, G., Favier, D. and Maresca, C., "Experimental and numerical study of the propeller/fixed wing interaction," *AIAA Journal of Aircraft*, Vol. 28, No. 6, 1991, pp. 365-373. https://doi.org/10.2514/3.46036.
26. Veldhuis, L.L., "Review of propeller-wing aerodynamic interference," 24th International Congress of the Aeronautical Sciences, Vol. 6, No. 1, 2004, pp. 2004-2006, Edinburgh, UK, Optimage Ltd. https://icas.org/icas_archive/icas2004/papers/065.pdf.
27. Witkowski, D.P., Lee, A.K. and Sullivan, J.P., "Aerodynamic interaction between propellers and wings," *AIAA Journal of Aircraft*, Vol. 26, No. 9, 1989, pp. 829-836. https://doi.org/10.2514/3.45848.
28. Mark, F.R., "Experimental Analysis of Propeller-Wing Interactions for a Micro Air Vehicle," *AIAA Journal of Aircraft*, Vol. 46, No. 1, 2009, pp. 65-73. https://doi.org/10.2514/1.34520.
29. de Vries, R., van Arnhem, N., Avallone, F., Ragni, D., Vos, R., Eitelberg, G. and Veldhuis, L.L., "Experimental investigation of over-the-wing propeller–boundary-layer interaction," *AIAA Journal*, Vol. 59, No. 6, 2021, pp. 2169-2182. https://doi.org/10.2514/1.J059770.
30. Greenblatt, D., "Unsteady low-speed wind tunnels," *AIAA Journal*, Vol. 54, No. 6, 2016, pp. 1817-1830. https://doi.org/10.2514/1.J054590.
31. "Image Stacks," *Adobe*, 15 Nov. 2022. https://helpx.adobe.com/il_en/photoshop/using/image-stacks.html.

32. Bachmann, M., Utehs, S., Vey, S., Paschereit, C.O. and Greenblatt, D., "Plasma-based active flow control on low Reynolds number airfoils," 49th Israel Annual Conference on Aerospace Sciences, 4-5 March 4, Tel Aviv, Haifa, 2009.
33. Greenblatt, D. and Washburn, A.E., "Influence of finite span and sweep on active flow control efficacy," *AIAA Journal*, Vol. 46, No. 7, 2008, pp. 1675-1694. https://doi.org/10.2514/1.33809.
34. Greenblatt, D., "Active control of tip-flap loads," *AIAA Journal*, Vol. 47, No. 3, 2009, pp. 783-788. https://doi.org/10.2514/1.37407.
35. Greenblatt, D., "Fluidic control of a wingtip vortex," *AIAA Journal*, Vol. 50, No. 2, 2012, pp. 375-386. http://doi.org/10.2514/1.57285.
36. "Motion Tracking in After Effects | Adobe." *Adobe*, https://www.adobe.com/il_en/products/aftereffects/motion-tracking.html.
37. De Troyer, T., Hasin, D., Keisar, D., Santra, S. and Greenblatt, D., "Plasma-Based Dynamic Stall Control and Modelling on an Aspect-Ratio-One Wing," *AIAA Journal* Vol. 60, No. 5, 2022, pp. 2905-2915. https://doi.org/10.2514/1.J060933.
38. Jackson, P. "Jane's all the world's aircraft 2003-2004," Coulsdon, UK, Jane's Information Group. ISBN 0710625375, 2003, pp. 588-589.
39. McGowan, R., Corke, T.C., Matlis, E.H., Kaszeta, R. and Gold, C., "Pulsed-DC plasma actuator characteristics and application in compressor stall control," AIAA Paper No. 2016-0394, 54th AIAA Aerospace Sciences Meeting, 4-8 January 2016, San Diego, CA. https://doi.org/10.2514/6.2016-0394.
40. Nudnova, M., Kindusheva, S., Aleksahdrov, N. and Starikovskiy, A., "Rate of plasma thermalization of pulsed nanosecond surface dielectric barrier discharge," AIAA Paper No. 2010-465, 48th AIAA Aerospace Sciences Meeting, 4 - 7 January 2010, Orlando, FL. https://doi.org/10.2514/6.2010-465.
41. Roupassov, D.V., Nikipelov, A.A., Nudnova, M.M. and Starikovskii, A. Yu., "Flow Separation Control by Plasma Actuator with Nanosecond Pulsed-Periodic Discharge, *AIAA Journal*, Vol. 47, No. 1, 2009, pp. 169-185. https://doi.org/10.2514/1.38113.
42. Lombardi, A.J., Bowles, P.O. and Corke, T.C., "Closed-loop dynamic stall control using a plasma actuator," *AIAA Journal*, Vol. 51, No. 5, 2013, pp. 1130-1141. https://doi.org/10.2514/1.J051988.

43. Garcia, M., Mongin, M. and Greenblatt, D., “Closed-loop stall control using pulsed DBD-plasma-actuation,” AIAA Paper No. 2025-0034, Scitech 2025 Forum, 6-10 January 2020, Orlando FL. https://doi.org/10.2514/6.2025-0034.